Published in final edited form as:

Mamm Genome. 2016 June ; 27(5-6): 200–212. doi:10.1007/s00335-016-9632-0.

A hypomorphic mutation of the gamma-1 adaptin gene (*Ap1g1*) causes inner ear, retina, thyroid, and testes abnormalities in mice

Kenneth R. Johnson[1], **Leona H. Gagnon**[1], and **Bo Chang**[1]

Kenneth R. Johnson: ken.johnson@jax.org

[1]The Jackson Laboratory, Bar Harbor, ME 04609, USA

Abstract

Adaptor protein (AP) complexes function in the intracellular sorting and vesicular transport of membrane proteins. The clathrin-associated AP-1 complex functions at the *trans*-Golgi network and endosomes, and some forms of this complex are thought to mediate the sorting of proteins in plasma membranes of polarized epithelial cells. A null mutation of the mouse *Ap1g1* gene, which encodes the gamma-1 subunit of the AP-1 complex, causes embryonic lethality when homozygous, indicating its critical importance in early development but precluding studies of its possible roles during later stages. Here, we describe our analyses of a new spontaneous mutation of *Ap1g1* named “figure eight” (symbol *fgt*) and show that it is an in-frame deletion of 6 bp, which results in the elimination of two amino acids of the encoded protein. In contrast to $Ap1g1^{-/-}$ null mice, mice homozygous for the recessive *fgt* mutation are viable with adult survival similar to controls. Although *Ap1g1* is ubiquitously expressed, the phenotype of $Ap1g1^{fgt}$ mutant mice is primarily restricted to abnormalities in sensory epithelial cells of the inner ear, pigmented epithelial cells of the retina, follicular epithelial cells of the thyroid gland, and the germinal epithelium of the testis, suggesting that impaired AP-1 sorting and targeting of membrane proteins in these polarized cells may underlie the observed pathologies. $Ap1g1^{fgt}$ mutant mice provide a new animal model to study the in vivo roles of gamma-1 adaptin and the AP-1 complex throughout development and to investigate factors that underlie its associated phenotypic abnormalities.

Introduction

Adaptor complexes promote the formation of clathrin-coated pits and vesicles and function in intracellular sorting and transport of membrane proteins (Ohno 2006). Humans and mice have four ubiquitously expressed adaptor protein complexes (AP-1, AP-2, AP-3, and AP-4), with additional diversification coming from their variable subunit compositions (Boehm and Bonifacino 2001). The heterote-trameric AP-1 complex is comprised of two large subunits termed adaptins (beta-1 and gamma-1), one medium (mu-type) subunit, and one small (sigma-type) subunit. Seven genetically distinct proteins of the AP-1 complex have been identified in mammals: AP1B1 (beta-1 adaptin), AP1G1 (gamma-1 adaptin), AP1M1

Correspondence to: Kenneth R. Johnson, ken.johnson@jax.org.

(mu1A), AP1M2 (mu1B), AP1S1 (sigma1A), AP1S2 (sigma1B), and AP1S3 (sigma1C). Although AP1G2 has sequence similarities with AP1G1, it does not interact with AP1B1 of the AP-1 complex and plays a functionally distinct role (Takatsu et al. 1998). AP1M1 is characteristic of the ubiquitous form of the AP-1 complex (AP-1A), whereas AP1M2 is found in the epithelium-specific AP-1B complex and confers different cargo-sorting functions. AP-1A plays a role in the sorting of integral membrane proteins at the *trans*-Golgi network (TGN) and endosomes, and AP-1B is thought to mediate polarized sorting of plasma membrane proteins in epithelial cells (Bonifacino 2014; Folsch et al. 1999; Nakatsu et al. 2014).

Most work on AP-1 complex function has been done using cell culture systems and in vitro analysis. Its role in intact organisms is less well understood, but growing evidence from animal models suggests that AP-1 deficits may be involved in the pathogenesis of disease (Nakatsu et al. 2014). Targeted knockout mutations of genes encoding AP-1 subunits in mice exhibit variable phenotypes. *Ap1s2*$^{-/-}$ mice are viable but have impaired synaptic vesicle recycling, reduced motor coordination, and impaired memory (Glyvuk et al. 2010). *Ap1m2*$^{-/-}$ mice, which lack the epithelial cell-specific AP-1B complex, exhibit 50 % lethality by 8 weeks of age, and surviving mice show growth retardation and sorting and polarity irregularities in intestinal epithelial cells (Hase et al. 2013). *Ap1m1*$^{-/-}$ mice die at embryonic day 13.5 (Meyer et al. 2000), and *Ap1g1*$^{-/-}$ mice die during the early blastocyst stage, at embryonic day 3.5 (Zizioli et al. 1999). The later stage of embryonic lethality in *Ap1m1*$^{-/-}$ mice compared with *Ap1g1*$^{-/-}$ mice may be because the loss of AP1M1 can be partially compensated for by AP1M2, whereas AP1G1 is required for the functional integrity of all AP-1 complex isoforms. The severe phenotype of the *Ap1g1* knockout mouse demonstrates the essential role that AP1G1 plays in early embryonic development but limits studies of its function at later stages of development.

Here, we report on the phenotype of adult mice that are homozygous for a hypomorphic mutation of *Ap1g1*. The new mutation arose spontaneously in a colony of mice at The Jackson Laboratory and was first identified by its associated circling behavior, which often indicates an inner ear dysfunction. The new recessive mutation was given the name “figure eight” (*fgt*) to reflect the atypical movement pattern of mutant mice (*fgt/fgt*). Further phenotypic analysis showed that *fgt/fgt* mice exhibit hearing loss as well as eye, thyroid, and testes defects. Genetic mapping and whole-exome sequencing analysis identified the *fgt* mutation as an in-frame 6 bp deletion in exon 13 of the *Ap1g1* gene, predicted to result in the loss of two amino acids in the translated protein. The *Ap1g1*^{fgt} mutant mice we describe here provide a new animal model for investigating the in vivo role of gamma adaptin and AP-1 adaptor complex function throughout development and into adulthood.

Materials and methods

Mice

All mice used in this study were produced and maintained in the Research Animal Facility of The Jackson Laboratory (Bar Harbor, ME), which is accredited by the American Association for the Accreditation of Laboratory Animal Care. The recessive figure-eight (*fgt*) mutation arose spontaneously in the C57BL/6-Tg (APOA1)1Rub/J colony (Stock No.

001927) at The Jackson Laboratory (JAX). Mutant mice were crossed to C57BL/6J mice and genotyped to select against the apolipoprotein A-1 transgene, and elimination of the transgene from the colony was subsequently confirmed. The newly established strain (C57BL/6-*Ap1g1*^{fgt}/Kjn, JAX Stock No. 006487) is maintained by breeding heterozygous +/*fgt* mice, identified by PCR genotyping. Mutant mice (*fgt/fgt*) can be identified without genotyping by their overt circling and head tilting behaviors.

Genetic mapping

To genetically map the *fgt* mutation, individual DNA samples from linkage cross mice were typed for multiple MIT microsatellite markers located throughout the mouse genome. Previously described PCR methods (Johnson et al. 2012) were used to genotype the chromosomal markers, which were then analyzed for co-segregation with the mutant phenotype. PCR primer pairs designed to amplify specific markers were purchased from Integrated DNA Technologies (Coralville, IA, USA).

Whole-exome sequencing

DNA purification, library construction, deep sequencing, and data quality control were performed by the Jackson Laboratory's Next Generation Sequencing service, and data analysis and annotation were performed by the Computational Sciences Biostatistics service. Purified genomic DNA from *fgt/fgt* mice and C57BL/6J controls were used to create libraries for whole-exome sequence capture.

DNA sequence confirmation and genotyping of the *fgt* mutation

PCR for comparative DNA analysis between *fgt* mutant and control mice was performed according to the same conditions as described above for genetic mapping. PCR primers used to genotype the *fgt* mutation of the *Ap1g1* gene were 5′-GAGTTTTGCCCTGGTGAATG-3′ (forward) and 5′-GCAAGGAAGATTCCAGATGC-3′ (reverse). PCR products (117 bp for the wild-type allele and 111 bp for the *fgt* allele) were separated on a 3.5 % agarose gel. For DNA sequence confirmation of genotypes, PCR products were purified with the QIAquick PCR Purification Kit (Qiagen Inc., Valencia, CA), and sequencing was performed using the same primers as for DNA amplification, then run on an applied biosystems 3700 DNA Sequencer with an optimized Big Dye Terminator Cycle Sequencing method.

Histopathology of inner ear, retina, thyroid gland, and testes

Anesthetized mice were perfused through the left ventricle of the heart with phosphate-buffered saline, followed by Bouin's fixative. Thyroid glands and testes were dissected out of the body, fixed in Bouin's for 7 days, and paraffin embedded. Inner ears were held in Bouin's fixative for 4 weeks before embedding. For eye preparations, mice were asphyxiated by carbon dioxide inhalation without perfusion. Enucleated eyes were fixed overnight in cold methanol/acetic acid solution (3:1, v/v), and paraffin embedded. All sections were mounted on glass slides and counterstained for microscopic examination. Sections of thyroid glands (6 μm), eyes (6 μm), and inner ears (4 μm) were stained with H&E. Sections of testes (5 μm) were stained with Periodic acid–Schiff (PAS) stain. All slides were examined on an

Olympus Optical BX40 light microscope (Olympus, Tokyo, Japan), and images were captured and processed utilizing the Olympus DP70 camera and software.

Assessment of hair cell morphology by SEM

Scanning electron microscopy was used to evaluate organ of Corti surface preparations. Inner ears were dissected from 14 *fgt* mutants and 14 control mice (postnatal ages 3, 15, 25, 40, and 77), fixed in 2.5 % glutaraldehyde in 0.1 M cacodylate for 4 h at 4 °C, and then subjected to two 10-min washes in 0.1 M phosphate buffer (pH 7.2). The outer shell of the cochlea and the stria vascularis were dissected away to expose the organ of Corti, and the sample was then post-fixed with osmium tetroxide–thiocarbohydrazide, dehydrated, and critical point dried (Self et al. 1998). After mounting, samples were sputter coated to produce a 15 nm gold coating and examined at 20 kV on a Hitachi 3000 N scanning electron microscope. Images were archived using Quartz.PCI (v5.1) software (Quartz, Vancouver, BC, Canada).

Auditory brainstem response (ABR) measurements

ABR thresholds were measured at 8, 16, and 32 kHz in a sound-attenuating chamber using the SmartEP auditory evoked potential diagnostic system from Intelligent Hearing Systems (IHS, Miami, FL) as described previously (Zheng et al. 1999). Briefly, mice were anesthetized with tribromoethanol (0.2 ml of 20 mg/ml stock per 10 g of body weight, i.p.) and placed on a temperature-controlled heating pad to maintain body temperature at 37 °C. Subdermal electrodes placed at the vertex and behind the ipsilateral and contralateral ears were used to record the ABR to tone bursts (3 ms duration. 1.5 ms cosine-gated rise/fall time) were amplified, filtered (100–3000 Hz), and averaged (25 kHz sampling rate, 10 ms analysis window). Stimulus intensity was initially decreased in 10 dB steps until the response began to disappear and then lowered in 5 dB steps; ABR threshold was defined as the lowest intensity at which an ABR response could be reliably obtained. Our average ABR thresholds for normal hearing mice are about 40, 20, and 45 dB SPL for 8, 16, and 32 kHz, respectively.

Clinical eye evaluation and fluorescein angiography

Eyes of all mice used in the characterization studies and linkage crosses were dilated with 1 % atropine ophthalmic drops (Bausch and Lomb Pharmaceuticals Inc., Tampa, FL) and were evaluated by Micron III in vivo bright field retinal imaging microscope equipped with image-guided optical coherence tomography (OCT) capabilities (Phoenix Laboratories, Inc). Fluorescein angiography (FA) was performed directly following imaging of the fundus. Fluorescein images were captured at 3–5 min after i.p. injection of 0.1 ml of 2 % fluorescein sodium (Akorn, Lake Forest, IL).

Electroretinography (ERG)

For electroretinographic evaluation of mutants, following an overnight dark adaptation, mice were anesthetized with an intraperitoneal injection of xylazine (80 mg/kg) and ketamine (16 mg/kg) in normal saline. Additional anesthetic was given if akinesia was inadequate. Briefly, dark-adapted, rod-mediated ERGs were recorded with the responses to short-wavelength

flashes over 4.0 log units to the maximum intensity by the photopic stimulator. Cone-mediated ERGs were recorded with white flashes after 10 min of complete light adaptation. The signals were sampled at 0.8 ms intervals and averaged.

T4 levels, body weights, and statistical analysis

For serum collection, mutant and control mice were exsanguinated, and whole blood was chilled on ice for 30 min, then centrifuged in a refrigerated bench top centrifuge for 10 min at 4 °C. At least 30 μl of serum was collected from each mouse and T4 levels were measured on a Beckman AU680 chemistry analyzer (Beckman Coulter, Inc. Brea CA), which permits automated measurements of T4. Body weights of female and male control and *fgt/fgt* mutant mice were measured between 4 and 6 weeks of age. The Student's *t* test (2-tailed, unequal variance) was used for statistical probability estimates in between-group comparisons of mean T4 levels and mean body weights.

Sperm collection and analysis

Sexually mature (aged >8 weeks) males were euthanized by cervical dislocation, and the cauda epididymides were removed from the body and placed in 1 ml PBS at 37 °C. Approximately 5–7 cuts were made in each epididymis to allow the sperm to swim out, and samples were incubated in PBS at 37 °C for 15 min. The samples were gently agitated, diluted 1:10 with warm PBS, and collected in a cannula for evaluation with the Integrated Visual Optical System, IVOS (Hamilton Thorne, Beverly MA).

Results

Phenotype and inheritance of the *fgt* mutation

The *fgt* mutation was first discovered in mice with circling and head tilting behaviors, and inheritance tests revealed that the mutant phenotype is recessive. Because the abnormal behaviors, including an inability to swim, indicated an impairment of inner ear function, mutant mice were examined for hearing impairment by ABR threshold measurements. Mutant (*fgt/fgt*, based on vestibular dysfunction) and non-mutant mice (+/+ or +/*fgt*) from the segregating B6-*fgt* colony were tested for ABR thresholds with 8, 16, and 32 kHz pure-tone stimuli (Fig. 1a). By 1 month of age, the average ABR thresholds of *fgt/fgt* mutant mice were statistically significantly higher than those of non-mutant controls, exhibiting about 40 dB threshold elevations at all frequencies. By 6 months of age, the *fgt/fgt* mice no longer produced a detectable ABR even at the maximum test stimulus of 100 dB. The hearing loss of *fgt/fgt* mice thus progresses from moderate to profound within a five-month post-wean period.

In addition to hearing and balance dysfunctions of the inner ear, mutant mice were found to have retinal degeneration, hyperplastic thyroid glands, and dysmorphic testis with reduced numbers and motility of sperm. A histological screen of tissue samples from other organs (including brain, spinal cord, muscle, heart, lung, liver, spleen, kidney, and bone) did not reveal any additional histological differences between mutant and control mice.

Genetic mapping

To determine the chromosomal location of the *fgt* mutation, two linkage crosses were generated by out-crossing C57BL/6 J mice with the *fgt* mutation (B6-*fgt*) to C3HeB/FeJ (C3H) mice. We produced 62 F2 progeny from an intercross of (B6-*fgt* X C3H) F1 hybrids and 73 N2 progeny from a backcross of (B6-*fgt* X C3H) F1 hybrids to B6-*fgt/fgt* mutant mice. Although the recessive *fgt* mutation was discovered by the circling behavior of homozygous mutants, the occurrence of this phenotype was lower than expected in the linkage cross mice. Because ABR thresholds were considered the most reliable method for identifying mutant mice, they were used to assign genotypes in the segregating intercross and backcross populations used for genetic linkage analysis. As can be seen from the scatter plots of ABR thresholds, mice with mutant (*fgt/fgt*) and mice with non-mutant (+/+ or +/*fgt*) genotypes fell into two distinct groups in both the intercross (Fig. 1b) and the backcross (Fig. 1c). As expected for a fully penetrant phenotype, about 25 % of the intercross mice (16/62) and 50 % of the backcross mice (35/73) had high ABR thresholds and were assigned *fgt/fgt* genotypes. Of the 35 N2 mice with high ABR thresholds (*fgt/fgt*), only 25 exhibited circling or head tossing behaviors, giving an estimate of 70 % penetrance for this phenotype in the backcross mice. Behaviors associated with vestibular dysfunction in mice are sometimes subtle and hard to recognize, which can account for the lower penetrance of this phenotype compared with the more dependable detection of auditory dysfunction by ABR threshold analysis.

Genome-wide linkage analysis of the F2 and N2 progeny from the two linkage crosses revealed a significant association of ABR thresholds with markers on Chr 8. Because *fgt/fgt* genotypes could be unambiguously classified (Fig. 1b, c), haplotype analysis with additional linkage markers was used to identify crossovers and refine the location of *fgt* between *D8Mit242* (101.7 Mb) and *D8Mit271* (114.4 Mb). About 160 protein-coding genes lie within this 13 Mb interval. The *Lcat* and *Calb2* genes were tested as possible candidates for *fgt*, but no DNA sequence differences between mutant and wild-type alleles were found in either gene.

Molecular identification of the *fgt* mutation and its predicted effects

Because candidate gene analysis failed to identify the *fgt* mutation, a next-generation whole-exome sequencing approach was undertaken. We focused the analysis of the exome sequence results on the 101.7–114.4 Mb region of Chr 8 where *fgt* was genetically mapped and identified 23 potential differences between B6- +/+ DNA and coiso-genic B6-*fgt/fgt* DNA that occur within exons (or flanking splice sites). All except one of the 23 putative differences had low mismatch ratios and heterozygous diploid consensus sequences, indicating that they were sequencing errors rather than actual DNA differences. Only one DNA sequence difference had a high mismatch ratio and a homozygous diploid consensus sequence as would be expected for the actual *fgt/fgt* mutation. A 6 bp deletion (TTTCTG) in the coding sequence of the *Ap1g1* gene was consistently detected in DNA from *fgt/fgt* mutants but not in DNA from +/+ control mice (Fig. 2a).

The 6 bp *fgt* deletion occurs in exon 13 of the *Ap1g1* cDNA reference sequence NM_009677 (encoding isoform one of the protein), which corresponds to exon 12 of the

NM_002301211 reference sequence (encoding isoform two). The deletion is predicted to be in-frame and result in the elimination of two amino acids (phenylalanine and leucine, Fig. 2b) at residues 391 and 392 of the isoform-1 protein (NP-033807), which correspond with residues 388 and 389 of the isoform-2 protein (NP-001288140). The deleted amino acids lie within the trunk or adaptin N-terminal homology domain (PF01602), which is involved in the interactions of AP1G1 with other subunits of the AP-1 complex (Boehm and Bonifacino 2001).

To confirm causality of the 6 bp deletion, we sequenced PCR-amplified DNA products from additional mutants (*fgt/fgt*) and B6 controls (+/+), and designed a PCR-based genotyping protocol (Fig. 2c). We then genotyped 22 mice from our segregating colony and verified that the *Ap1g1* genotypes (+/+, +/*fgt*, and *fgt/fgt*) of all mice corresponded with their phenotypes.

The unusual nature of the 6 bp deletion may have originated from genomic instability caused by a nearby inverted repeat sequence, a mechanism that has been implicated in inducing deletions, translocations, and duplications (Voineagu et al. 2008). A perfect inverted repeat sequence of the *fgt*-deleted region was detected at the most 3′ end of exon 13 (Fig. 2b). The two inverted repeats could thus form a hairpin loop structure and stall replication, which may then have led to the ancestral 6 bp deletion. Our PCR results (Fig. 2d) lend support to this possibility. PCR primers designed to amplify wild-type DNA containing both inverted repeat sequences produced two differently sized products representing distinct conformational forms, the larger product likely the result of hairpin formation. When the same primers were used to amplify DNA from *fgt/fgt* mice (containing only one of the inverted repeat sequences), only a single product was observed.

Inner ear pathology

To determine the pathological basis of the hearing impairment and vestibular dysfunction of *fgt/fgt* mice, inner ears were examined for histological abnormalities by light and electron microscopy. Cross sections of cochlea from +/+ and *fgt/fgt* mice were examined by light microscopy at 1 and 3 months of age (Fig. 3). No differences were detected in cochlear structures at 1 month of age, but at 3 months of age the organ of Corti, comprised of the hair cells and supporting cells of the sensory epithelia, appeared to have completely degenerated in the *fgt/fgt* mutant cochlea (Fig. 3). A gradual degeneration of the organ of Corti and loss of hair cells could explain the progressive hearing loss observed in *fgt/fgt* mutant mice (Fig. 1).

For a higher resolution examination of this cochlear pathology, scanning electron microscopy (SEM) was used to visualize surface preparations of the organ of Corti (Fig. 4). At 1 week of age, no signs of outer or inner hair cell degeneration were detected in the cochlea of *fgt/fgt* mutant mice (Fig. 4b) as compared with +/+ control mice (Fig. 4a). At 5 weeks of age, all hair cells of the +/+ control cochlea appeared normal (Fig. 4c, e, g), whereas some of the outer hair cells in the *fgt/fgt* cochlea were missing stereocilia bundles (Fig. 4d, f, h), indicating cellular degeneration. The frequency of outer hair cell bundle loss was greater near the apex (Fig. 4d) and the base (Fig. 4h) than in the mid region (Fig. 4f) of the cochlea. A disruption of outer hair cell patterning also was observed in a small region of

the cochlea near the apex (Fig. 4d). Inner hair cells appeared normal in cochlea of *fgt/fgt* mutant mice at both 1 and 5 weeks of age. These results indicate that organ of Corti degeneration in *fgt/fgt* mutant mice begins with a loss of outer hair cells sometime between 1 and 5 weeks of age.

In addition to cochlear hair cell loss, a loss of vestibular hair cells also was observed in *fgt/fgt* mutant mice (data not shown). We detected missing vestibular hair cells by cross-sectional analysis of the crista ampullaris, the sensory organ of rotation located in the semicircular canal of the inner ear, and loss of these sensory hair cells could explain the vestibular dysfunction of the mutant mice.

Eye pathology

Eye examination of control mice (genotype: +/*fgt*) showed a normal retinal structure by OCT (Fig. 5a), a normal fundus (Fig. 5b), no fluorescein leakage in the retina (Fig. 5c), and a normal retina by histology (Fig. 5d) at 6 weeks of age. Examination of the eyes from *fgt/fgt* mutant mice by OCT, however, revealed noticeable retinal abnormalities (Fig. 5e, i). Scattered depigmented spots were seen in the fundus of *fgt/fgt* mice at 6 weeks of age (Fig. 5f), which developed into large depigmented areas by 16 weeks of age (Fig. 5j). Fluorescein angiography showed a pattern of choroidal neovascularization (CNV) with multiple areas of leakage (Fig. 5g, k). Newly formed vessels in the retina were detected by histology at 6 (Fig. 5h) and 16 (Fig. 5l) weeks of age. Despite these retinal abnormalities, standardized electroretinograms of mutant mice had normal amplitudes, indicating that there was no retinal degeneration by 16 weeks of age.

Thyroid-related abnormalities

Compared with the normal thyroid histology of +/+ or +/*fgt* control mice (Fig. 6a), the thyroid glands of *fgt/fgt* mutant mice have few normal follicles containing colloid material but have many highly proliferating epithelial cells (Fig. 6b) that give rise to thyroid adenomas or goiters. As might be expected from the extensive thyroid gland abnormalities, serum T4 levels of *fgt/fgt* mice are lower than those of controls, especially at a young age (Fig. 6c). The mean T4 level (± SEM) was 6.2 ± 0.4 μg/dl for 15 control females and 6.2 ± 06 μg/dl for seven control males tested at 3–40 weeks of age. The mean T4 level was 2.2 ± 0.3 μ/dl for 11 *fgt/fgt* females and 3.2 ± 0.3 μ/dl for 12 males, a small but statistically significant difference (prob < 0.05). Regardless of sex, the low T4 values of *fgt/fgt* mice were highly significantly different from those of control mice (prob < 0.001), which could account for the smaller size of *fgt/fgt* mutants compared with control mice. At 4–6 weeks of age, female *fgt/fgt* mice weighed on average 5.9 g less than female controls, and male *fgt/fgt* mice weighed on average 3.0 g less than male controls (Fig. 6d). The weights of mutant mice were statistically significantly lower than those of control mice (prob < 0.001 for females and prob < 0.05 for males).

Testes and sperm abnormalities

Testes of *fgt/fgt* mice displayed a disorganized germinal epithelium (Fig. 7). All meiotic stages are present in the seminiferous tubules of mutant mice, from proliferating spermatogonia to elongated spermatids being released from the seminiferous epithelium;

however, the number of maturing sperm cells is reduced in mutant mice. Compared with minimum standard values for normal mice, *fgt/fgt* mutant mice have a reduced total concentration of spermatozoa (12.1 vs 20 M/ml) and reduced sperm motility (61 vs 70 %). Approximately 30–50 % of mature spermatozoa have tails bent at the mid-piece. Mutant males are considered sub-fertile because, though reduced in number, enough motile spermatozoa are produced for occasional successful impregnation.

Discussion

Mice homozygous for a null mutation of *Ap1g1* die at embryonic day 3.5, and heterozygous mice display a reduced growth rate during nursing but no other abnormalities (Zizioli et al. 1999). In contrast, *fgt/fgt* mutant mice are viable and exhibit multiple phenotypic abnormalities, providing a means to investigate the in vivo cellular function of AP1G1 and the AP-1 complex in tissues of later stage embryos and adults. Rather than causing a total loss of AP-1 function, the $Ap1g1^{fgt}$ mutation may alter the binding affinity of gamma adaptin with other AP-1 subunits thereby altering the protein cargo selection or intracellular transport function of the complex. The two amino acids deleted by the *fgt* mutation (Fig. 2) are within the NH2-terminal domain trunk region of gamma adaptin (residues 24–577 of NP_033807), which is the part of the protein shown to interact with the mu and sigma subunits of AP-1 (Page and Robinson 1995).

Human genetic disorders have been associated with mutations of genes encoding the sigma-type subunit of AP-1 but not with the mu-type subunit or the beta or gamma adaptins. *AP1S1* mutations cause MEDNIK (mental retardation, enteropathy, deafness, peripheral neuropathy, ichthyosis, and keratoderma) syndrome (Montpetit et al. 2008); *AP1S2* mutations are responsible for some forms of X-linked mental retardation (Tarpey et al. 2006); and *AP1S3* mutations increase susceptibility to pustular psoriasis (Setta-Kaffetzi et al. 2014). Deafness is one of the identifying characteristics of MEDNIK syndrome, and the reported interaction of AP1S1 (also known as AP19) with AP1G1 (Page and Robinson 1995) suggests the possibility that the deafness associated with the mouse $Ap1g1^{fgt}$ mutation may be caused by a decreased ability of mutant AP1G1 to interact with AP1S1. Although no pathologic *AP1G1* mutations have been reported in human populations, our results suggest that undetected hypomorphic *AP1G1* mutations may be contributing risk factors for sensorineural hearing impairment, neovascular retinopathy, thyroid dysfunction, and male infertility.

The AP-1 complex has been implicated in the establishment of planar cell polarity (PCP), and the knockdown of gamma-1 adaptin in HeLa cells resulted in an abnormal accumulation of the VANGL2 protein at the TGN (Guo et al. 2013). VANGL2 is critical to the establishment of PCP in auditory hair cells and stereociliary bundle orientation is severely disrupted in *Vangl2* mutant mice (Montcouquiol et al. 2003); however, the orientation and patterning of hair cells is normal in *fgt/fgt* mutant mice (Fig. 4) indicating that the $Ap1g1^{fgt}$ mutation does not affect PCP in these cells.

One of the functions ascribed to AP-1 is the transport and sorting of proteins from the TGN or endosomes to different plasma membrane domains of polarized cells. Studies in zebrafish

provide evidence that AP-1-mediated localization of membrane proteins in sensory epithelial cells plays a role in maintaining auditory and balance function (Nakatsu et al. 2014). Mutations in the gene encoding the beta-1 subunit of AP-1 (*ap1b1*) of zebrafish cause a progressive degeneration of the sensory epithelium of the inner ear and lateral line organs (Clemens Grisham et al. 2013), similar to the inner ear pathology we observed in *Ap1g1*^{fgt} mutant mice (Figs. 3, 4). Na^+/K^+ ATPase, a plasma membrane enzyme that is essential for maintaining sodium and potassium concentration gradients and polarized membrane potentials, requires AP-1 for proper targeting to the plasma membrane (Efendiev et al. 2008). Na^+/K^+ ATPase was mislocalized to the apical rather than basolateral surface of sensory hair cells in the *ap1b1* mutant zebrafish and was thought to underlie their auditory and balance dysfunction (Clemens Grisham et al. 2013). Na^+/K^+ ATPase has been localized to cochlear and vestibular cells in the mouse inner ear (Erichsen et al. 1996; Schulte and Steel 1994) and, although the zebrafish mutations occur in the beta rather than the gamma subunit of AP-1, a similar pathological mechanism may underlie the progressive hearing loss and hair cell degeneration that we observed in *Ap1g1*^{fgt} mutant mice.

Mislocalization of epithelial cell membrane proteins such as Na^+/K^+ ATPase may also be a common underlying mechanism that could account for the defects we observed in the retina, thyroid gland, and testes of *Ap1g1*^{fgt} mutant mice. *Ap1g1*^{fgt} mutant mice develop early neovascular lesions in the retina and provide a reliable animal model for studying factors that initiate retinal angiogenesis, subretinal neovascularization, and choroidal vascular anastomosis formation. Ocular angiogenesis is a central pathologic component in a large number of serious human ocular diseases. In the retina, subretinal neovascularization occurs as a serious complication in about ten percent of age-related macular degeneration (AMD) patients (Ferris et al. 1984). Complications of neovascularization are a principal cause of vision loss in AMD patients, and the complication creates a sudden visual disability in the affected patients. Retinal pigment epithelial cells (RPE) play a vital role in the pathogenesis of AMD (Zarbin 2004). The RPE is a cuboidal hexagonal monolayer comprising the outermost layer of the retina; its apical portion faces the outer segments of photoreceptor cells, and its basolateral surface interacts with the choriocapillaris. RPE cells are polarized epithelial cells that have Na^+/K^+ ATPase localized on their apical surface (Rizzolo 1999). The very low-density lipoprotein receptor (VLDLR) also has been localized in the plasma membrane of RPE cells, and *Vldlr* mutations in mice (Heckenlively et al. 2003; Hu et al. 2008) lead to subretinal neovascularization similar to that seen in *Ap1g1*^{fgt} mutant mice.

The thyroid glands of *fgt/fgt* mice are characterized by a loss of thyroid follicles with a consequent deficiency of thyroid hormone and an impaired growth rate (Fig. 6). Establishment and maintenance of epithelial surface polarity is essential to normal thyroid function. Thyroid follicular cells are polarized epithelial cells that coordinate several oppositely located surface enzyme activities, and epithelial surface asymmetry is regulated largely by intracellular sorting of newly synthesized membrane proteins at the TGN (Kuliawat et al. 1995). The mislocalization of Na^+/K^+-ATPase, which has been localized in the baso-lateral membrane of follicular cells (Nakamura et al. 1999), or other membrane proteins may underlie the thyroid pathology of *Ap1g1*^{fgt} mutant mice.

The developing sperm cells and Sertoli cells of the germinal epithelium of the testes appear to be disorganized in *Ap1g1*^{fgt} mutant mice (Fig. 7), and sperm have an overall reduction in numbers and motility. Mammalian Sertoli cells are polarized with apical and basolateral plasma membranes (Nakagawa et al. 2004), and spermatozoa are highly polarized cells whose surface membrane can be divided into functionally, structurally, and biochemically distinct domains (Bearer and Friend 1990). The alpha four isoform of Na^+K^+-ATPase, which has been shown to play critical role in sperm mobility (Woo et al. 2000), is significantly upregulated during spermatogenesis, and its cellular distribution is modified with development, being diffusely expressed at the plasma membrane and intracellular compartments of immature cells and subsequently localized to the midregion of the spermatozoon flagellum (Wagoner et al. 2005).

That the multiple pathologies associated with the hypomorphic *Ap1g1*^{fgt} mutation may be the result of mis-localized membrane proteins in polarized cells of the affected tissues is consistent with the intracellular sorting and transport role of AP-1; however, other mechanisms may be involved and additional studies are needed. The *Ap1g1*^{fgt} mutant mice provide a valuable model for examining the in vivo roles of gamma-1 adaptin and the AP-1 complex and the pathological mechanisms underlying the observed inner ear hair cell degeneration, subretinal neovascularization, thyroid follicle loss, and germinal epithelium disorganization.

Acknowledgments

We thank Sandra Gray for mouse colony management and generation of linkage cross mice, Chantal Longo-Guess and Cong Tian for ABR threshold measurements, Norm Hawes for eye examinations, Mary Ann Handel for help interpreting testes pathology, and Jane Farley for CASA analysis. This research was supported by US National Institutes of Health (NIH) Grants DC004301 (KRJ) and EY019943 (BC). The Jackson Laboratory institutional shared services are supported in part by NIH National Cancer Institute Support Grant CA34196.

References

Bearer EL, Friend DS. Morphology of mammalian sperm membranes during differentiation, maturation, and capacitation. J Electron Microsc Tech. 1990; 16:281–297. [PubMed: 2250184]

Boehm M, Bonifacino JS. Adaptins: the final recount. Mol Biol Cell. 2001; 12:2907–2920. [PubMed: 11598180]

Bonifacino JS. Adaptor proteins involved in polarized sorting. J Cell Biol. 2014; 204:7–17. [PubMed: 24395635]

Clemens Grisham R, Kindt K, Finger-Baier K, Schmid B, Nicolson T. Mutations in ap1b1 cause mistargeting of the Na(+)/K(+)-ATPase pump in sensory hair cells. PLoS One. 2013; 8:e60866. [PubMed: 23593334]

Efendiev R, Budu CE, Bertorello AM, Pedemonte CH. G-protein-coupled receptor-mediated traffic of Na, K-ATPase to the plasma membrane requires the binding of adaptor protein 1 to a Tyr-255-based sequence in the alpha-subunit. J Biol Chem. 2008; 283:17561–17567. [PubMed: 18420589]

Erichsen S, Zuo J, Curtis L, Rarey K, Hultcrantz M. Na, K-ATPase alpha- and beta-isoforms in the developing cochlea of the mouse. Hear Res. 1996; 100:143–149. [PubMed: 8922988]

Ferris FL 3rd, Fine SL, Hyman L. Age-related macular degeneration and blindness due to neovascular maculopathy. Arch Ophthalmol. 1984; 102:1640–1642. [PubMed: 6208888]

Folsch H, Ohno H, Bonifacino JS, Mellman I. A novel clathrin adaptor complex mediates basolateral targeting in polarized epithelial cells. Cell. 1999; 99:189–198. [PubMed: 10535737]

Glyvuk N, Tsytsyura Y, Geumann C, D'Hooge R, Huve J, Kratzke M, Baltes J, Boening D, Klingauf J, Schu P. AP-1/sigma1B-adaptin mediates endosomal synaptic vesicle recycling, learning and memory. EMBO J. 2010; 29:1318–1330. [PubMed: 20203623]

Guo Y, Zanetti G, Schekman R. A novel GTP-binding protein-adaptor protein complex responsible for export of Vangl2 from the trans Golgi network. Elife. 2013; 2:e00160. [PubMed: 23326640]

Hase K, Nakatsu F, Ohmae M, Sugihara K, Shioda N, Takahashi D, Obata Y, Furusawa Y, Fujimura Y, Yamashita T, Fukuda S, Okamoto H, Asano M, Yonemura S, Ohno H. AP-1B-mediated protein sorting regulates polarity and proliferation of intestinal epithelial cells in mice. Gastroenterology. 2013; 145:625–635. [PubMed: 23684748]

Heckenlively JR, Hawes NL, Friedlander M, Nusinowitz S, Hurd R, Davisson M, Chang B. Mouse model of subretinal neovascularization with choroidal anastomosis. Retina. 2003; 23:518–522. [PubMed: 12972764]

Hu W, Jiang A, Liang J, Meng H, Chang B, Gao H, Qiao X. Expression of VLDLR in the retina and evolution of subretinal neovascularization in the knockout mouse model's retinal angiomatous proliferation. Invest Ophthalmol Vis Sci. 2008; 49:407–415. [PubMed: 18172119]

Johnson KR, Longo-Guess CM, Gagnon LH. Mutations of the mouse ELMO domain containing 1 gene (Elmod1) link small GTPase signaling to actin cytoskeleton dynamics in hair cell stereocilia. PLoS One. 2012; 7:e36074. [PubMed: 22558334]

Kuliawat R, Lisanti MP, Arvan P. Polarized distribution and delivery of plasma membrane proteins in thyroid follicular epithelial cells. J Biol Chem. 1995; 270:2478–2482. [PubMed: 7852309]

Meyer C, Zizioli D, Lausmann S, Eskelinen EL, Hamann J, Saftig P, von Figura K, Schu P. mu1A-adaptin-deficient mice: lethality, loss of AP-1 binding and rerouting of mannose 6-phosphate receptors. EMBO J. 2000; 19:2193–2203. [PubMed: 10811610]

Montcouquiol M, Rachel RA, Lanford PJ, Copeland NG, Jenkins NA, Kelley MW. Identification of Vangl2 and Scrb1 as planar polarity genes in mammals. Nature. 2003; 423:173–177. [PubMed: 12724779]

Montpetit A, Cote S, Brustein E, Drouin CA, Lapointe L, Boudreau M, Meloche C, Drouin R, Hudson TJ, Drapeau P, Cossette P. Disruption of AP1S1, causing a novel neurocutaneous syndrome, perturbs development of the skin and spinal cord. PLoS Genet. 2008; 4:e1000296. [PubMed: 19057675]

Nakagawa A, Nagaosa K, Hirose T, Tsuda K, Hasegawa K, Shiratsuchi A, Nakanishi Y. Expression and function of class B scavenger receptor type I on both apical and basolateral sides of the plasma membrane of polarized testicular Sertoli cells of the rat. Dev Growth Differ. 2004; 46:283–298. [PubMed: 15206959]

Nakamura N, Suzuki Y, Sakuta H, Ookata K, Kawahara K, Hirose S. Inwardly rectifying K + channel Kir7.1 is highly expressed in thyroid follicular cells, intestinal epithelial cells and choroid plexus epithelial cells: implication for a functional coupling with Na + , K +-ATPase. Biochem J. 1999; 342(Pt 2):329–336. [PubMed: 10455019]

Nakatsu F, Hase K, Ohno H. The role of the clathrin adaptor AP-1: polarized sorting and beyond. Membranes (Basel). 2014; 4:747–763. [PubMed: 25387275]

Ohno H. Clathrin-associated adaptor protein complexes. J Cell Sci. 2006; 119:3719–3721. [PubMed: 16959901]

Page LJ, Robinson MS. Targeting signals and subunit interactions in coated vesicle adaptor complexes. J Cell Biol. 1995; 131:619–630. [PubMed: 7593184]

Rizzolo LJ. Polarization of the Na + , K(+)-ATPase in epithelia derived from the neuroepithelium. Int Rev Cytol. 1999; 185:195–235. [PubMed: 9750268]

Schulte BA, Steel KP. Expression of alpha and beta subunit isoforms of Na, K-ATPase in the mouse inner ear and changes with mutations at the Wv or Sld loci. Hear Res. 1994; 78:65–76. [PubMed: 7961179]

Self T, Mahony M, Fleming J, Walsh J, Brown SD, Steel KP. Shaker-1 mutations reveal roles for myosin VIIA in both development and function of cochlear hair cells. Development. 1998; 125:557–566. [PubMed: 9435277]

Setta-Kaffetzi N, Simpson MA, Navarini AA, Patel VM, Lu HC, Allen MH, Duckworth M, Bachelez H, Burden AD, Choon SE, Griffiths CE, Kirby B, Kolios A, Seyger MM, Prins C, Smahi A,

Trembath RC, Fraternali F, Smith CH, Barker JN, Capon F. AP1S3 mutations are associated with pustular psoriasis and impaired Toll-like receptor 3 trafficking. Am J Hum Genet. 2014; 94:790–797. [PubMed: 24791904]

Takatsu H, Sakurai M, Shin HW, Murakami K, Nakayama K. Identification and characterization of novel clathrin adaptor-related proteins. J Biol Chem. 1998; 273:24693–24700. [PubMed: 9733768]

Tarpey PS, Stevens C, Teague J, Edkins S, O'Meara S, Avis T, Barthorpe S, Buck G, Butler A, Cole J, Dicks E, Gray K, Halliday K, Harrison R, Hills K, Hinton J, Jones D, Menzies A, Mironenko T, Perry J, Raine K, Richardson D, Shepherd R, Small A, Tofts C, Varian J, West S, Widaa S, Yates A, Catford R, Butler J, Mallya U, Moon J, Luo Y, Dorkins H, Thompson D, Easton DF, Wooster R, Bobrow M, Carpenter N, Simensen RJ, Schwartz CE, Stevenson RE, Turner G, Partington M, Gecz J, Stratton MR, Futreal PA, Raymond FL. Mutations in the gene encoding the sigma 2 subunit of the adaptor protein 1 complex, AP1S2, cause X-linked mental retardation. Am J Hum Genet. 2006; 79:1119–1124. [PubMed: 17186471]

Voineagu I, Narayanan V, Lobachev KS, Mirkin SM. Replication stalling at unstable inverted repeats: interplay between DNA hairpins and fork stabilizing proteins. Proc Natl Acad Sci USA. 2008; 105:9936–9941. [PubMed: 18632578]

Wagoner K, Sanchez G, Nguyen AN, Enders GC, Blanco G. Different expression and activity of the alpha1 and alpha4 isoforms of the Na, K-ATPase during rat male germ cell ontogeny. Reproduction. 2005; 130:627–641. [PubMed: 16264093]

Woo AL, James PF, Lingrel JB. Sperm motility is dependent on a unique isoform of the Na, K-ATPase. J Biol Chem. 2000; 275:20693–20699. [PubMed: 10764792]

Zarbin MA. Current concepts in the pathogenesis of age-related macular degeneration. Arch Ophthalmol. 2004; 122:598–614. [PubMed: 15078679]

Zheng QY, Johnson KR, Erway LC. Assessment of hearing in 80 inbred strains of mice by ABR threshold analyses. Hear Res. 1999; 130:94–107. [PubMed: 10320101]

Zizioli D, Meyer C, Guhde G, Saftig P, von Figura K, Schu P. Early embryonic death of mice deficient in gamma-adaptin. J Biol Chem. 1999; 274:5385–5390. [PubMed: 10026148]

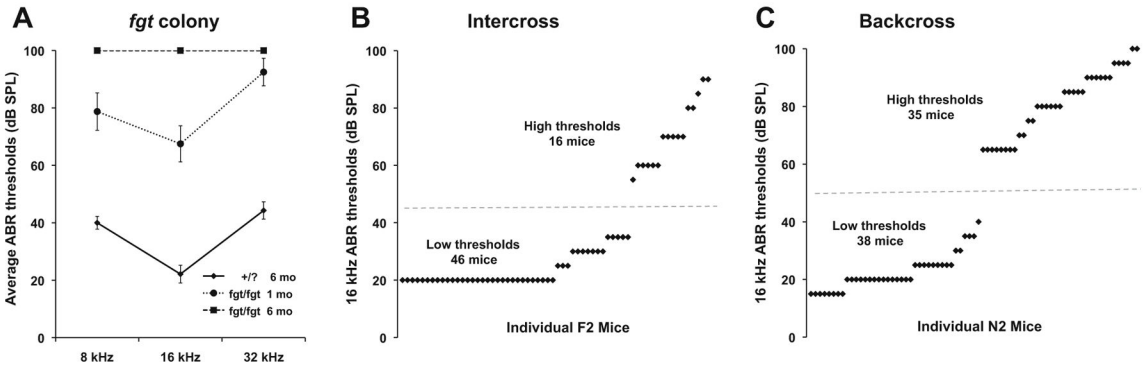

Fig. 1.

ABR thresholds of *fgt/fgt* mutants and linkage cross mice. **a** ABR threshold means (± SEM) of mutant and non-mutant mice from the B6-*fgt* segregating colony. ABR thresholds are shown for four mutant mice (*fgt/fgt*) tested at 1 and 6 months of age, and seven non-mutant control mice (+/*fgt* or +/+, shown as +/?) tested at 6 months of age. **b.** *Scatter plot* of ABR thresholds of F2 mice from an intercross of (B6-*fgt* X C3HeB/FeJ) F1 hybrids tested at 7–11 weeks of age (avg 9.5 weeks). **c** *Scatter plot* of ABR thresholds of 73 N2 mice from a backcross of (B6-*fgt* X C3HeB/FeJ) F1 hybrids to B6-*fgt/fgt* mutants tested at 6–17 weeks of age (avg 8.5 weeks). Each *black diamond* represents an individual mouse. The *horizontal dashed line* demarks the division between low (non-mutants) and high (*fgt/fgt* mutants) threshold groups

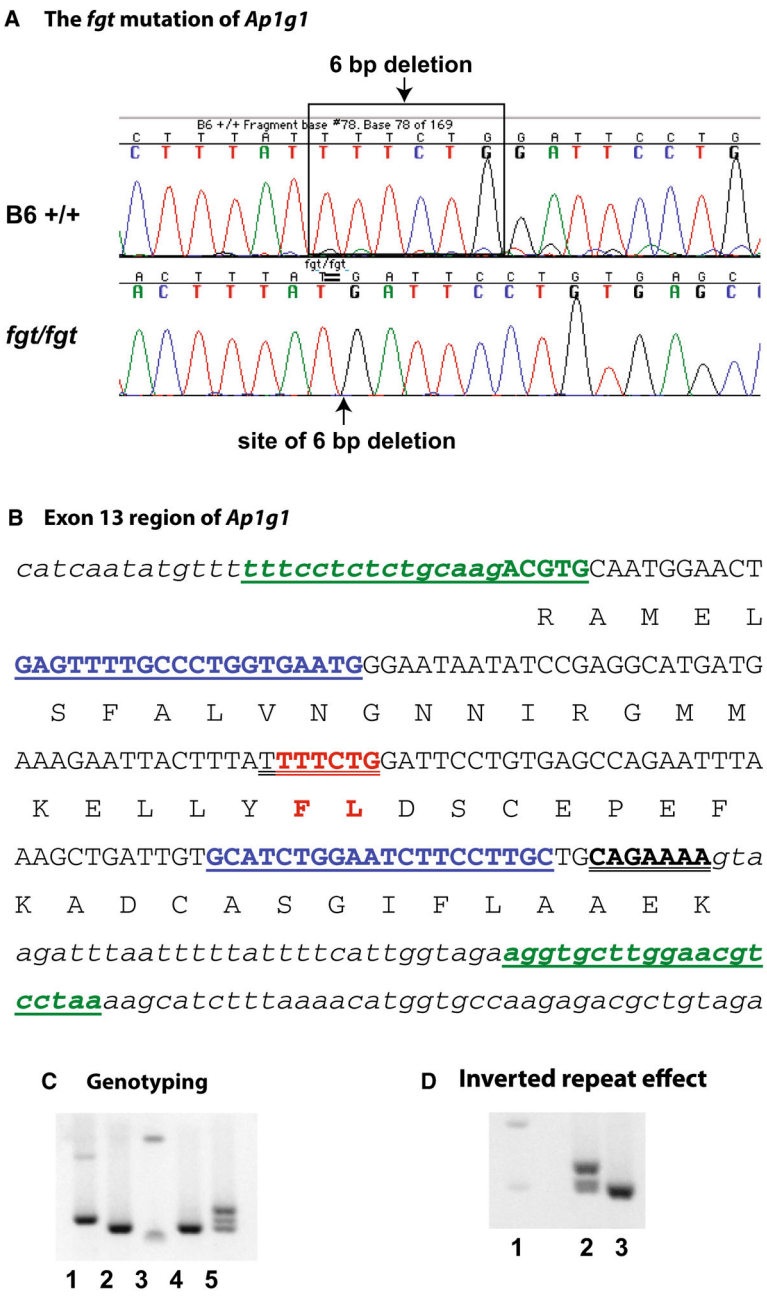

Fig. 2.

The *fgt* mutation of *Ap1g1* and its consequences. **a** DNA sequencing chromatograms of control B6 +/+ and mutant *fgt/fgt* mice showing that the *fgt* mutation is a 6 bp deletion in the *Ap1g1* gene. **b** The six base pairs deleted in the *fgt* mutation (shown in *red*) are in exon 13 of the NM_009677 reference sequence. The exon sequence is shown in capital letters and flanking intron sequences are shown in small case, *italic font*. Amino acids are shown below the second nucleotide of the corresponding codons. The in-frame 6 bp deletion is predicted to eliminate the phenylalanine (F) and leucine (L) amino acids shown in *red*. Underlined sequences in *blue font* correspond to the PCR primers used for mutation sequence

confirmation and genotyping, and underlined sequences in *green font* correspond to the PCR primers used to examine the conformational effect of the two 7 bp inverted repeat sequences (*double underlined*). **c** PCR genotyping results using the *blue underlined* primer sequences shown in **b**. *Ap1g1* genotypes for +/+ B6 control (*lane* 1), *fgt/fgt* (*lanes* 2 and 4) and +/*fgt* (*lane* 5) mice are shown with reference to 100 and 200-bp size *markers* (*lane* 3). An extra heteromeric band can be seen in the +/*fgt* genotype of *lane* 5. **d** PCR results using the *green underlined* primers shown in B, which flank both inverted repeat sequences were predicted to amplify a 207 bp product in +/+ DNA (*lane* 2) and a 201 bp product in *fgt/fgt* DNA (*lane* 3), with reference to 200 and 300 bp size markers (*lane* 1). The large extra band seen in *lane* 2 but absent from *lane* 3 is a conformational isoform of the wild-type PCR product, presumably a consequence of the two inverted repeat sequences

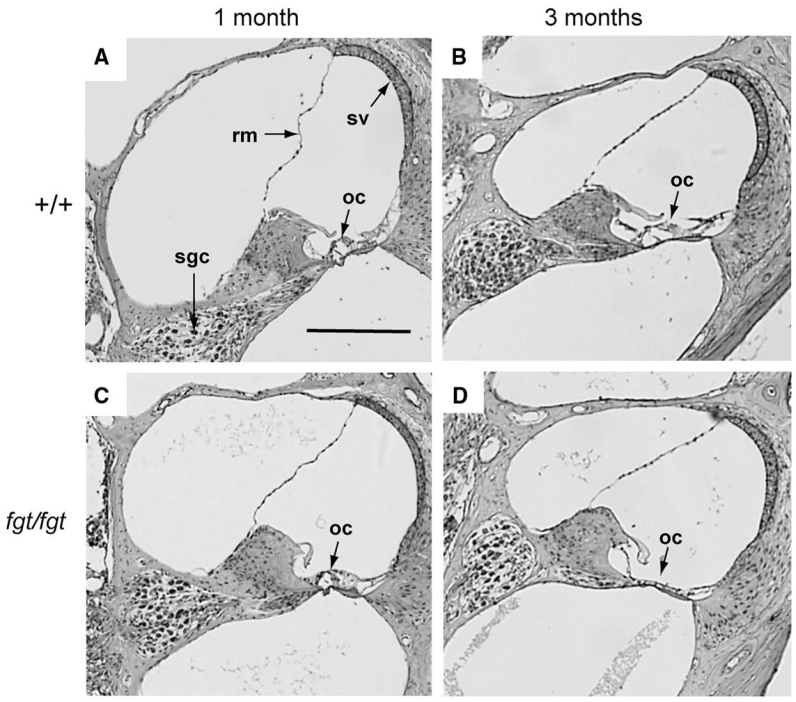

Fig. 3.

Organ of Corti degeneration in *Ap1g1*^{fgt} mutant mice. Mid-modiolar cross sections through the cochlea of +/+ control (**a**, **b**) and *fgt/fgt* mutant (**c**, **d**) mice were examined at 1 and 3 months of age. 1-month sections (**a**, **c**) are through the basal turn, and 3-month sections (**b**, **c**) are through the middle turn of the cochlea. Structural features of the cochlea are labeled in the 1-month +/+ section (**a**): Reissner's membrane (rm), stria vascularis (sv), spiral ganglion cells (sgc), and organ of Corti (oc). The organ of Corti, labeled in all panels, is intact in 1- and 3-month-old controls (**a**, **b**) and in 1-month-old mutants (**c**), but has degenerated in 3-month-old mutants (**d**). All *sections* are shown at the same magnification; the *black scale bar* in *panel* A represents 200 micrometers

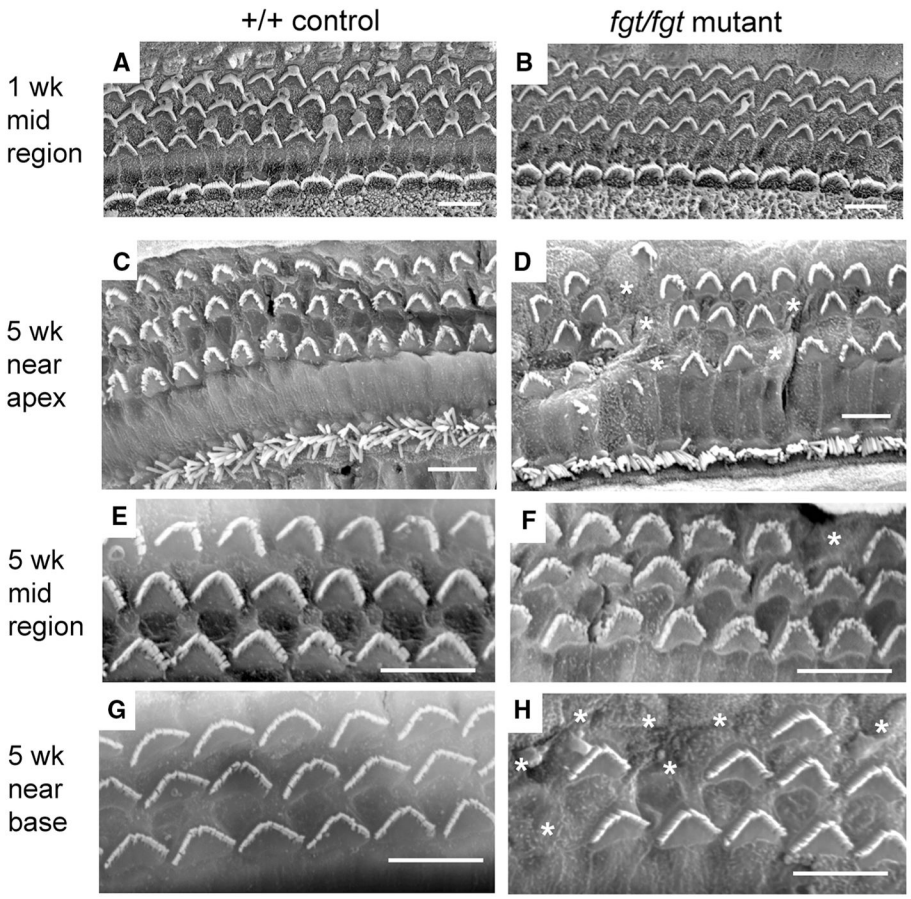

Fig. 4.

Progressive hair cell loss in *Ap1g1*^{fgt} mutant mice. SEM was used to examine surface preparations of the organ of Corti in cochleae from +/+ control (**a**, **c**, **e**, **g**) and *fgt/fgt* mutant (**b**, **d**, **f**, **h**) mice at 1 week (**a**, **b**) and 5 weeks (**c–h**) of age. In *panels* A–D outer hair cells constitute the top three rows and inner hair cells the bottom row, only outer hair cells are shown in *panels* E–H. At 1 week of age, no differences in outer or inner hair cell bundle morphology or survival were observed between control (**a**) and mutant (**b**) cochleae. In mutant cochleae at 5 weeks of age (**d**, **f**, **h**) stereociliary bundles (marked with *asterisks*) were missing in outer hair cells but not inner hair cells. Loss of outer hair cell bundles was more frequent near the apex (**d**) and near the base (**h**) than in the mid region of the cochlea (**f**). Sporadic regions near the apex also exhibited a disrupted patterning of outer hair cell bundles (left-most part of **d**). *Black scale bars* at lower right of each panel represent 10 micrometers

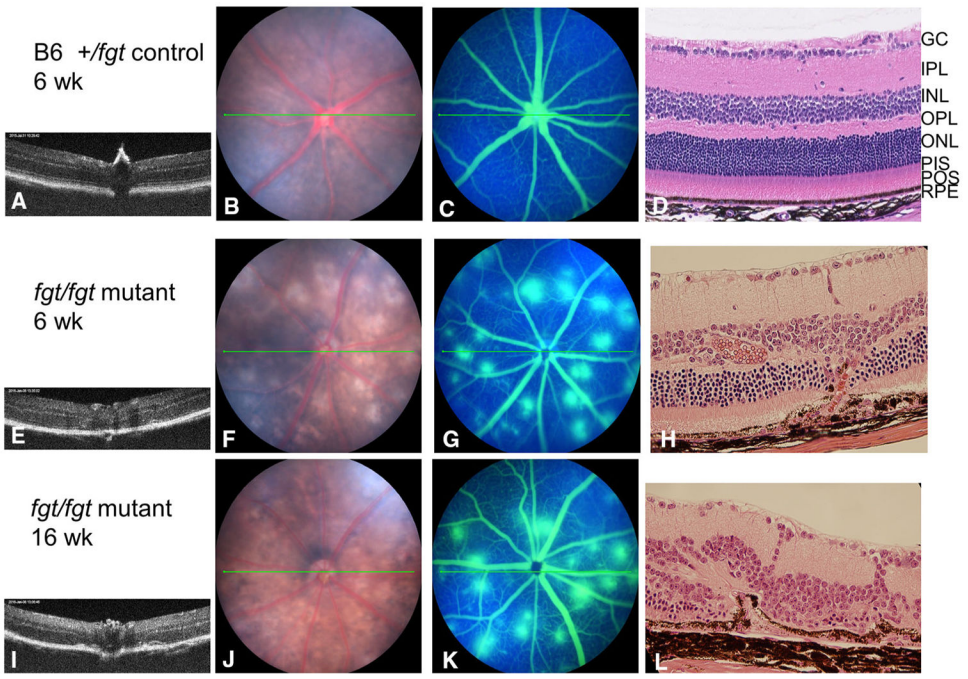

Fig. 5.

Retinal spots and choroidal neovascularization in *Ap1g1*^{fgt} mutant mice. The eye examination of the control mice (genotype: +/*fgt*) showed a normal retinal structure by OCT (**a**), normal fundus (**b**), no fluorescein leakage in the retina (**c**), and a normal retina by histology (**d**) at 6 weeks of age. But examination of the *fgt/fgt* mutant mice revealed the abnormal retina by OCT at 6 weeks of age (**e**) and at 16 weeks of age (**i**), a scattered depigmented spots fundus at 6 weeks of age (**f**), and the large depigmented areas fundus at 16 weeks of age (**j**). The fluorescein angiography showed the areas of leakage in the retina as a typical fluorescein angiographic pattern of CNV at 6 weeks of age (**g**) and at 16 weeks of age (**k**). The neovessels were detected by histology at 6 weeks of age (**h**) and at 16 weeks of age (**l**). Retinal layers are labeled in the +/*fgt* control mouse (**d**): *GCL* ganglion cell layer; *IPL* inner plexiform layer; *INL* inner nuclear layer; *OPL* outer plexiform layer; *ONL* outer nuclear layer; *PIS* photoreceptor inner segment; *POS* photoreceptor outer segment; *RPE* retina pigment epithelium

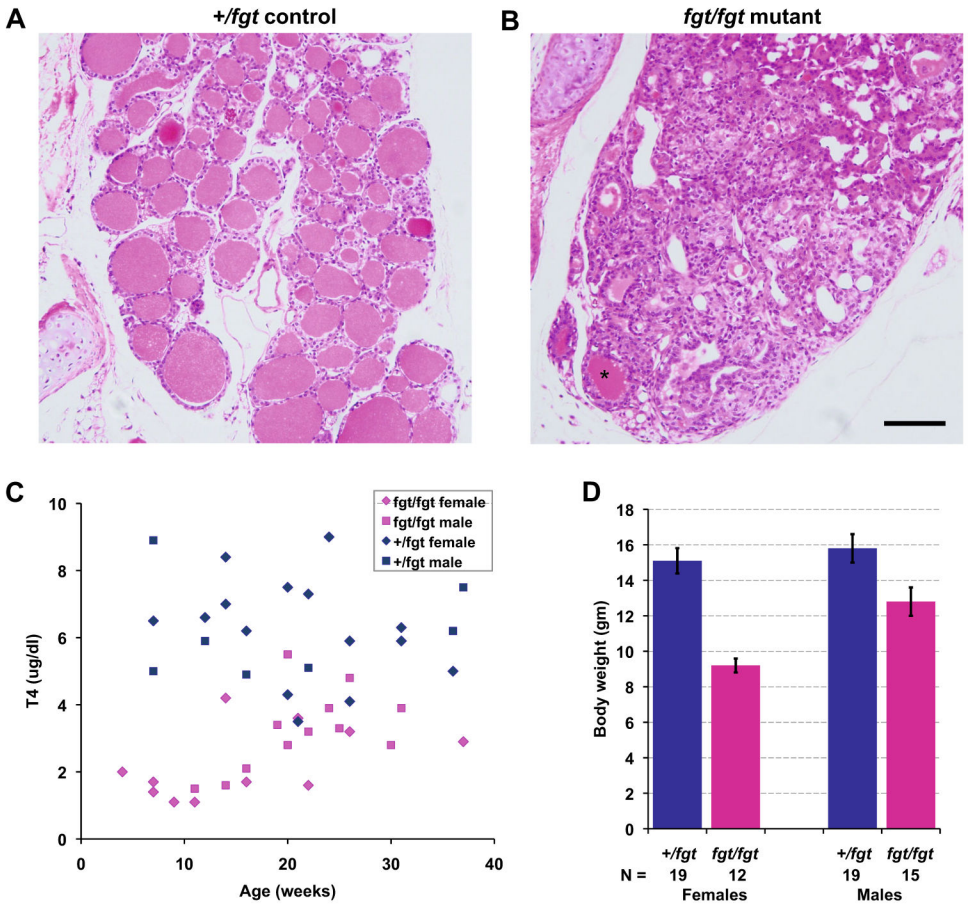

Fig. 6.

Thyroid gland pathology and its effects in *Ap1g1*^{fgt} mutant mice. **a**, **b** Cross sections of thyroid glands stained with H&E from a 15-week-old +/*fgt* control (**a**) and an age-matched *fgt/fgt* mutant mouse (**b**). Thyroid glands of mutant mice have only a few normal follicles containing colloid material (*asterisk* in B) and have highly proliferating epithelial cells that give rise to adenomas (goiters). A and B are the same magnification; the *black scale bar* in B represents 100 micrometers. (**c**) *Scatter plot* of thyroxine (T4) levels in +/*fgt* control (15 females, 7 males) and *fgt/fgt* mutant mice (11 females, 12 males) from 3–40 weeks of age. Mutant mice have lower T4 levels than controls especially at younger ages. (**d**) The mean body weights (*error bars*, ± SEM) of female and male control and mutant mice were compared at 4–6 weeks of age

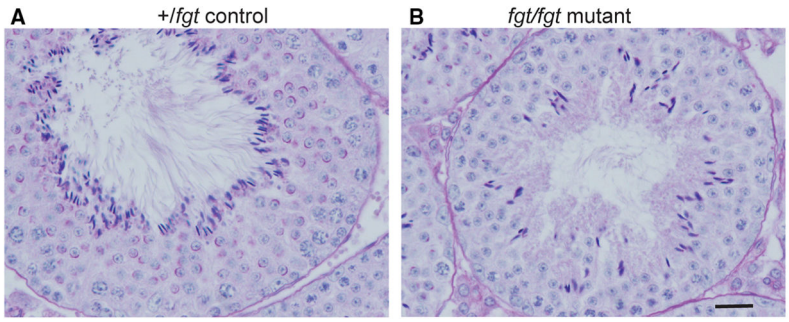

Fig. 7.

Testes pathology in *Ap1g1*^{fgt} mutant mice. PAS-stained cross sections of testes from a 3-month-old +/*fgt* control (**a**) and an age-matched *fgt/fgt* mutant mouse (**b**) reveal striking differences in the histological structure of the seminiferous epithelium. Compared with controls, mutant tubules show a disorganized arrangement of sperm cells and Sertoli cells and contain fewer elongated spermatids (darkly stained cells bordering the lumen). A and B are the same magnification; the *black scale bar* in B represents 20 micrometers